

Tetravalent SARS-CoV-2 Neutralizing Antibodies Show Enhanced Potency and Resistance to Escape Mutations

Shane Miersch^{1,8}, Zhijie Li^{2,8}, Reza Saberianfar¹, Mart Ustav³, Levi Blazer¹, Chao Chen¹, Wei Ye¹, Alia Pavlenco¹, Suryasree Subramania¹, Serena Singh¹, Lynda Ploder¹, Safder Ganaie⁴, Daisy Leung⁴, Rita E. Chen⁴, James Brett Case⁴, Guiseppe Novelli⁵, Giulia Matusali⁶, Francesca Colavita⁶, Maria R. Copabianchi⁶, Suresh Jain⁷, J.B. Gupta⁷, Gaya Amarasinghe⁴, Michael Diamond⁴, James Rini^{2,*}, Sachdev S. Sidhu^{1,*}

Affiliations

1 - The Donnelly Centre, University of Toronto, Toronto, Canada

2 - Department of Biochemistry, University of Toronto, Toronto, Canada

3 - Icosagen, Õssu, Estonia

4 - Department of Medicine, Washington University School of Medicine, St. Louis, MO, USA

5 - Department of Biomedicine and Prevention, Tor Vergata University of Rome, 00133, Rome, Italy

6 - Laboratory of Virology, National Institute for Infectious Diseases "L. Spallanzani" IRCCS, Rome, Italy

7 - Virna Therapeutics, West Roxbury, MA, USA

8 - The authors contributed equally

*** - Corresponding author**

Corresponding authors email: james.rini@utoronto.ca and sachdev.sidhu@utoronto.ca

ABSTRACT

Recombinant neutralizing antibodies (nAbs) derived from recovered patients have proven to be effective therapeutics for COVID-19. Here, we describe the use of advanced protein engineering and modular design principles to develop tetravalent synthetic nAbs that mimic the multi-valency exhibited by IgA molecules, which are especially effective natural inhibitors of viral disease. At the same time, these nAbs display high affinity and modularity typical of IgG molecules, which are the preferred format for drugs. We show that highly specific tetravalent nAbs can be produced at large scale and possess stability and specificity comparable to approved antibody drugs. Moreover, structural studies reveal that the best nAb targets the host receptor binding site of the virus spike protein, and thus, its tetravalent version can block virus infection with a potency that exceeds that of the bivalent IgG by an order of magnitude. Design principles defined here can be readily applied to any antibody drug, including IgGs that are showing efficacy in clinical trials. Thus, our results present a general framework to develop potent antiviral therapies against COVID-19, and the strategy can be readily deployed in response to future pathogenic threats.

INTRODUCTION

As of October 30, 2020, the ongoing COVID-19 viral pandemic has tallied more than 44,000,000 confirmed infections and caused over 1,100,000 deaths (www.who.int). Moreover, the highly infectious nature of the disease has imposed severe economic hardship across the world due to the need for social distancing and lockdown measures. Despite intensive global efforts, no effective vaccines have yet been approved, and a number of repurposed drugs have shown only limited or uncertain efficacy^{1,2}. Thus, there is an urgent need for potent targeted therapies that can inhibit the SARS-CoV-2 virus directly, by blocking either its entry into host cells or its replication and subsequent release from cells.

Several lines of evidence suggest that SARS-CoV-2 neutralizing antibodies (nAbs) that bind directly to the virus and inhibit entry into host cells have therapeutic potential. First, many infected individuals either remain asymptomatic or recover rapidly with only minimal symptoms, and the plasma from these patients usually contains nAbs^{3,4}. Second, transfer of plasma containing nAbs from convalescent patients to symptomatic patients has been beneficial in some cases⁵⁻⁷. Third, recombinant nAbs that inhibit the interaction between SARS-CoV-2 and host cells confer protection in cell-based assays and animal models^{8,9}, and efficacy has also been observed for nAbs targeting the related coronaviruses SARS-CoV¹⁰⁻¹² and MERS¹³. Consequently, a number of nAbs have entered clinical trials as post-infection treatment of COVID-19 associated with SARS-CoV-2 (Clinicaltrials.gov - [NCT04452318](https://clinicaltrials.gov/ct2/show/study/NCT04452318), [NCT04497987](https://clinicaltrials.gov/ct2/show/study/NCT04497987)).

SARS-CoV-2 virions contain 25-100 glycosylated spike (S) proteins that protrude from the virus surface^{14,15}. Surface-associated S proteins bind to angiotensin-converting enzyme 2 (ACE2) to mediate host cell entry¹⁶. The S protein contains two subunits (S1 and S2) and forms a homotrimer. The receptor binding domain (RBD), located in the C-terminal region of the S1 subunit, recognizes ACE2 on host cells; binding facilitates cleavage of the S2 subunit by cell-surface proteases, which in turn promotes fusion and internalization of the virus¹⁶. The most potent nAbs against both SARS-CoV-2 and SARS-CoV block ACE2 through direct competition for binding to the RBD¹⁷⁻²¹. Consequently, we focused our efforts on developing Abs that bound to the RBD and competed with ACE2.

To date, all clinically advanced candidate nAbs against SARS-CoV-2 infection have been derived by cloning from B-cells of recovered COVID-19 patients or from other natural sources^{9,17,19–23}. Here, we applied an alternative strategy using *in vitro* selections with phage-displayed libraries of synthetic Abs built on a single human framework derived from the highly validated drug trastuzumab. This approach enabled the rapid production of high affinity nAbs with properties optimized for drug development. Moreover, the use of a highly stable framework enabled facile and modular design of ultra-high affinity nAbs in tetravalent formats that retained favorable drug-like properties and exhibited neutralization potencies that greatly exceeded those of the bivalent IgG format. These methods provide a general means to rapidly improve the potency of virtually any nAb targeting SARS-CoV-2 and its relatives, and thus, our strategy can be applied to improve COVID-19 therapies and can be adapted in response to future pathogenic threats.

RESULTS

Engineering of anti-RBD Fabs and IgGs

Using a phage-displayed human antigen-binding fragment (Fab) library similar to the highly validated library F²⁴, we performed four rounds of selection for binding to the biotinylated RBD of SARS-CoV-2 immobilized on streptavidin-coated plates. Screening of 384 clones for binding to CoV-2 RBD, revealed 348 Fab-phage clones that bound to the RBD but not to streptavidin. Fab-phage were screened by ELISA and those that exhibited >50% loss in binding to RBD in the presence of 200 nM ACE2 were sequenced, revealing 34 unique clones (**Fig. 1A**), deemed to be potential nAbs and converted into the full-length human IgG1 format for purification and functional characterization.

To estimate affinities, ELISAs were performed with serial dilutions of IgG protein binding to biotinylated S protein trimer captured with immobilized streptavidin, and these assays showed that three IgGs bound with EC₅₀ values in the sub-nanomolar range (**Fig. 1B,C and Table 1**). ELISAs also confirmed that each IgG could partially block the binding of biotinylated ACE2 to immobilized S protein (**Fig. 1D**). Moreover, similar to the highly specific IgG trastuzumab, ELISAs showed that the three IgGs did not bind to seven immobilized proteins that are known to exhibit high non-specific binding to some IgGs, and lack of binding to these proteins has been shown to be predictive of good pharmacokinetics *in vivo* (**Fig. 1E**)^{25,26}. We also used biolayer interferometry (BLI) to measure binding kinetics and determine avidities more accurately, and all three antibodies exhibited sub-nanomolar dissociation constants (**Table 1, Fig. S1**), in close accord with the estimates determined by ELISA. IgG 15033 exhibited the highest avidity, which was mainly due to a two- or seven-fold faster on-rate than IgG 15031 or 15032, respectively, and thus, we focused further efforts on this Ab.

We took advantage of the precision design of our synthetic Ab library to rapidly improve the affinity of Ab 15033. The synthetic library was designed with tailored diversification of key positions in all three heavy chain complementarity-determining regions (CDRs) and the third CDR of the light chain (CDR-L3). Consequently, we reasoned that the already high affinity of Ab 15033 could be further improved by recombining the heavy chain with a library of light chains with naïve diversity in CDR-L3. Following selection for binding to the RBD, the light chain library yielded

numerous variants, 17 of which were purified in the IgG format and analyzed by BLI (**Fig. S2**). Several of the variant light chains resulted in IgGs with improved binding compared with IgG 15033, and in particular, IgG 15033-7 (**Fig. 1B**) exhibited significantly improved avidity ($K_D = 300$ or 39 pM, respectively) due to an off-rate that was an order of magnitude slower (**Table 1, Fig. S2**).

Structural analysis of Fabs in complex with the RBD and the S protein

To understand the molecular basis for antagonism of ACE2 binding, we solved the X-ray crystal structures of the SARS-CoV-2 RBD in complex with Fab 15033 or 15033-7 at 3.2 or 3.0 Å resolution, respectively (**Fig. 2A**). As expected, backbone superposition showed that the two complexes were essentially identical (RMSD = 0.17 Å). However, there were differences in side chain interactions due to sequence differences in the CDR-L3 loop, which explained the enhanced affinity of Fab 15033-7 compared with Fab 15033 (**Fig. 2B**). Although the side chains of Tyr^{108L} in Fab 15033 and His^{108L} in Fab 15033-7 both make hydrogen bonds with the side chain of Tyr⁴⁷³ in the RBD, the bond mediated by His^{108L} is shorter, and thus, likely to be stronger. Moreover, in Fab 15033-7, the side chain of His^{108L} also makes an intramolecular hydrogen bond with the side chain of Thr^{109L}, which Tyr^{108L} and Arg^{109L} are incapable of making in Fab 15033, and this interaction may stabilize the CDR-L3 loop of Fab 15033-7 in a conformation that is favorable for antigen recognition. Thus, the crystal structures show that the two substitutions in the CDR-L3 loop of Fab 15033-7 relative to Fab 15033 act in a cooperative manner to mediate favorable intermolecular contacts with the RBD, and also, intramolecular interactions that stabilize the loop in a conformation that may be better positioned to interact with the RBD.

We next analyzed the structures to understand how the Abs could function as antagonists of RBD binding to ACE2. Binding of Fab 15033-7 to the RBD involves an extensive interface, with 1130 and 1112 Å² of surface area buried on the epitope or paratope, respectively, and 59% or 41% of the structural paratope is formed by the light or heavy chain, respectively (**Fig. 2C**). Comparison of the Fab and ACE2 epitopes on the RBD revealed extensive overlap, with 79% or 69% of the Fab or ACE2 epitope occluded by the other ligand (**Fig. 2C**). Thus, direct steric hinderance explains the blockade of ACE2 binding by Fabs 15033 and 15033-7 (**Fig. 1D**).

We also used cryogenic electron microscopy to visualize Fab 15033 in complex with the S protein trimer (**Fig. S3A**). This analysis revealed that all three RBDs in a single trimer were positioned in an “up” conformation, which was similar to the conformation bound to ACE2, and the three RBDs were bound to three Fab molecules. Notably, the C-termini of the three Fabs were positioned close to each other and pointed away from the S protein, suggesting that a single IgG may be able to present two Fabs in a manner that would enable simultaneous engagement of two RBDs on a single S protein. Indeed, this was confirmed in single particle negative stain electron micrographs of IgG 15033 and the S protein, which revealed that the two Fabs of a single IgG bound two RBDs on a single S protein trimer with a pincer-like grip (**Fig. S3B**). Taken together, the X-ray crystallography and electron microscopy showed that Fabs 15033 and 15033-7 block ACE2 binding to RBD by direct steric hinderance, and simultaneous binding of Fabs to multiple RBDs on the S protein trimer enables the IgGs to inhibit ACE2 binding with enhanced potency due to avidity.

Engineering of tetravalent nAbs with enhanced avidities

Next, we explored whether we could further enhance the avidity of nAbs by taking advantage of modular design strategies to engineer tetravalent formats. Each SARS-CoV-2 particle displays multiple S protein trimers, suggesting that multivalent Fab binding could enhance avidity, especially since a single IgG 15033 molecule can utilize both Fab arms to bind a single S protein trimer. We reasoned that additional Fab arms added to an IgG may further enhance avidity by interacting with RBDs on S protein trimers close to the trimer engaged by the core IgG. Thus, we designed tetravalent versions of 15033 and 15033-7 by fusing additional Fabs to either the N- or C- terminus of the IgG heavy chain to construct molecules termed Fab-IgG or IgG-Fab, respectively (**Fig. 3A**). Consistent with our hypothesis, the tetravalent molecules exhibited higher avidity, and consequently, greatly reduced off rates compared with their bivalent counterparts, and dissociation constants were in the low single-digit picomolar range (**Fig. 3B, Table 1**).

Our ultimate aim was to produce therapeutic Abs that could be used to treat COVID-19 in patients. Aside from high affinity and specificity, effective Ab drugs must also possess favorable

biophysical properties including high yields from recombinant expression in mammalian cells, high thermodynamic stability, and lack of aggregation and excessive hydrophobic surface area. All IgGs and tetravalent molecules were produced in high yields by transient expression in Expi293F cells (160-200 mg/L, **Table 1**). All proteins were highly thermostable with melting temperatures of the CH3/Fab domain ranging from 81-87 °C, which exceeded the melting temperature of the trastuzumab Fab (79.5 °C, **Table 1**). Size exclusion chromatography revealed that all IgGs eluted as a predominant monodisperse single peak with elution volumes nearly identical to that of trastuzumab (**Fig. 3C and Table 1**), and the monomeric fraction was calculated to be 91 to >95% (**Table 1**). All tetravalent molecules also eluted as single peaks in advance of trastuzumab, consistent with their larger molecular weights. IgG and tetravalent versions of both 15033 and 15033-7 could be purified to near homogeneity by protein-A affinity chromatography, as evidenced by SDS-PAGE (**Fig. 3D**). Taken together, these analyses demonstrate that the IgGs and their tetravalent derivatives possess good drug-like biophysical properties, which should facilitate drug development at large scale.

Inhibition of SARS-CoV-2 infection in cell-based assays

We assessed the effects of the nAbs on virus infection in a neutralization assay that measured the infection of ACE2-expressing Vero E6 cells with the SARS-CoV-2 strain 2019-nCoV/USA_WA1/2020. All three high affinity nAbs from the naïve library (**Fig. 1**) exhibited dose-dependent neutralization of SARS-CoV-2 infection, confirming their neutralization capacity (**Table 1**). Consistent with affinities, IgG 15033 was most potent with an IC₅₀ of 3.5 nM, and its potency was confirmed with the observation of strong neutralization of a second SARS-CoV-2 strain (2019-nCoV/Italy-INMI1, data not shown). Moreover, the tetravalent Fab-IgG and IgG-Fab versions of 15033 exhibited improved potencies with IC₅₀ values of 320 or 320 pM, respectively (**Fig. 4A and Table 1**). The optimized IgG 15033-7 also exhibited high neutralizing potency with an IC₅₀ of 790 pM and its tetravalent Fab-IgG and IgG-Fab versions exhibited the best potencies of all molecules tested with IC₅₀ values of 100 or 61 pM, respectively. Taken together, these results showed that naïve synthetic Ab libraries can yield highly potent nAbs with excellent drug-

like properties, and further optimization and engineering of tetravalent formats can produce drug-like molecules with ultra-high potencies beyond those of bivalent IgGs.

Resistance to potential viral escape mutants

To explore neutralization of potential escape mutants, we generated HIV-gag-based lentivirus-like particle (VLPs) pseudotyped with the SARS-CoV-2 S protein. We confirmed ACE2-dependent uptake of the pseudotyped VLPs by HEK-293 cells stably over-expressing exogenous ACE2, and we showed that uptake was inhibited by either Fc-tagged RBD (RBD-Fc) or IgG 15033. Within this system, we generated a panel of 44 pseudotyped VLP variants, each containing a single alanine substitution at an RBD position within or close to the ACE2-binding site. Twenty of these VLP variants exhibited a >4-fold reduction in internalization compared with the wild-type (wt) VLP, suggesting that these wt side chains contributed favorably to the interaction between the RBD and ACE2. The remaining 24 VLP variants were internalized with high efficiency, and these represent good mimics of escape mutants, which maintain strong ACE2-mediated infectivity but may potentially reduce binding to nAbs that compete directly with ACE2.

With the panel of 24 VLP variants that mimicked potential escape mutants, we surveyed the effects on cellular uptake after treatment with various nAbs (**Fig. 4B**). We defined as escape mutants those VLP variants for which cellular uptake in the presence of 50 nM nAb was >5% of the uptake in the absence of the nAb. Based on this definition, we found that 6 of the mutations enabled escape from IgG 15033, whereas only three mutations enabled escape from IgG 15033-7. Presenting the 15033 paratope in tetravalent formats resulted in nAbs that could neutralize more variants than IgG 15033, and most importantly, tetravalent nAbs containing the 15033-7 paratope strongly neutralized all variants except one. As expected, these results showed that enhancing the avidity of the IgG paratope for the S protein enhanced both potency and resistance to escape mutations. Moreover, similar enhancements were also achieved by the presentation of paratopes in tetravalent rather than bivalent formats, and the most effective nAbs were those that presented the optimized paratope in the tetravalent format.

DISCUSSION

SARS-CoV-2 has wreaked havoc on global health and economics, and along with its relatives SARS-CoV and MERS, has shown that viral outbreaks and pandemics will continue to plague the world in the future. Consequently, it is essential for the scientific community to adapt the most advanced drug development technologies to combat not only COVID-19, but also, pathogenic disease in general. In this context, we have deployed advanced synthetic antibody engineering to rapidly develop human nAbs, which are potent therapeutic candidates in the natural IgG format, and are even better neutralizing agents in the synthetic tetravalent formats that our modular design strategies enable. Most importantly, the enhanced affinities and potencies afforded by tetravalent nAbs are achieved without compromising any of the favorable characteristics that make IgG molecules ideal drugs. Moreover, tetravalent nAbs resist potential escape mutants, which further augments the power of these molecules as drugs to combat not only SARS-CoV-2, but also, its relatives that may emerge in the future.

COVID-19 has also exposed the need for drug development to respond to viral outbreaks in real time, to prevent the global spread of viral pathogens to the point where a pandemic threatens the entire global community. In this regard, the most rapid method for drug development to combat COVID-19 has proven to be the manufacture of nAbs isolated from infected patients by B cell cloning. Several reports have now shown that these technologies can deliver drug-grade therapeutic nAbs for manufacturing and subsequent clinical trials in approximately six months^{17,27}. These extraordinarily rapid drug development timelines set a benchmark for alternative technologies.

With our platform, we show that synthetic *in vitro* antibody engineering holds up well against B cell cloning, both in terms of speed and quality of drug development. Our project was initiated at the beginning of April, 2020 when we identified our first naïve Ab leads targeting the SARS-CoV-2 S protein. Within a month, we had validated lead IgG molecules as neutralizing agents in cell-based assays with authentic virus. In parallel, we initiated further selections to optimize the Fab 15033 paratope, which yielded our best lead nAb 15033-7, and we reformatted this lead in to the tetravalent formats that further enhanced potency. By the beginning of October, we had established manufacturing-grade stable cells capable of producing multi-gram

quantities of drug-grade nAbs from a litre of culture, in both the IgG and tetravalent formats. We are now manufacturing our best nAb for clinical trials. Thus, we have shown that synthetic Ab engineering technologies can match the six-month lead-to-manufacture timelines established by methods based on cloning of natural nAbs, and further improvements are possible by further streamlining of key development steps.

Moreover, synthetic engineering technologies hold key advantages over natural cloning methods. First, synthetic engineering offers exquisite control over Ab design; as we have shown, optimal frameworks and diversity designs can ensure that candidate therapeutics possess biophysical properties that are ideal for drug development. Also, the use of highly stable frameworks facilitates the rapid construction of complex tetravalent formats that enhance potency while retaining favorable drug-like properties. Perhaps most importantly, synthetic methods can overcome a fundamental limitation of technologies that depend on natural repertoires, namely, the need for infected patients as a source of drug leads. By its very nature, B cell cloning is a reactive technology that can only be implemented once a viral outbreak is underway, and this places a fundamental limit on the time required for drug development. With synthetic *in vitro* methods, drug development can proceed in a proactive manner, as development and stockpiling of potential therapeutics in advance of outbreaks is feasible. Indeed, large-scale sequencing efforts have provided unprecedented access to the genomes of thousands of SARS-CoV-2 relatives and other pathogens that may be poised to cause future outbreaks^{28,29}. With our methods, we have shown that it is feasible to develop synthetic Abs targeting hundreds of antigens in parallel³⁰, and thus, it is entirely feasible to target in advance the myriad pathogens that may pose future health risks. Working within a collaborative international network, we have initiated efforts with this aim.

METHODS AND MATERIALS

Cells

Cells were maintained in humidified environments at 37 °C in 5% CO₂ in the indicated media. Vero E6 (ATCC), HEK293T (ATCC) and HEK293T cells stably overexpressing ACE2 were maintained at 37 °C in 5% CO₂ in DMEM containing 10% (vol/vol) FBS. Expi293F cells (ThermoFisher) were maintained at 37 °C in 8% CO₂ in Expi293F expression media (ThermoFisher).

Protein Production

The previously reported piggyBac transposase-based expression plasmid PB-T-PAF³¹ containing a CMV promotor (PB-CMV) and a woodchuck hepatitis virus posttranscriptional regulatory element (WPRE) was used for large-scale transient expression. cDNA encoding the SARS-CoV-2 spike ectodomain trimer (residues 1-1211), followed by a foldon trimerization motif³², a 6xHis tag and an AviTag biotinylation motif³³ was cloned in to the PB-CMV vector using standard molecular biology techniques and residues 682–685 (RRAR) and 986–987 (KV) were mutated to SSAS and two proline residues to remove the furin cleavage site on the SARS-CoV-2 spike protein and stabilize the pre-fusion form of the spike³⁴, respectively. The SARS-CoV-2 receptor binding domain (RBD, residues 328-528), the soluble human ACE2 construct (residues 19-615), and the SARS-CoV RBD (residues 315-514), each followed by a 6xHis tag and an AviTag, were similarly cloned in to the same vector. For expression, PB-CMV expression constructs were mixed with Opti-MEM media (Gibco) containing 293fectin reagent (Thermo Fisher) and the mixture incubated for 5 min before addition to the shaker flask containing 10⁶ Freestyle 293-F cells/mL grown in suspension in Freestyle 293 expression media (Thermo Fisher). Expression was allowed to continue for 6 days before purification.

Protein purification and *in vitro* biotinylation

Expressed proteins were harvested from expression medium by binding to Ni-NTA affinity resin eluted with 1X PBS containing 300 mM imidazole and 0.1% (v/v) protease inhibitor cocktail (Sigma), then further purified by size-exclusion chromatography. For the RBDs and ACE2, a

Superdex 200 Increase (GE healthcare) column was used. For the spike ectodomain, a Superose 6 Increase (GE healthcare) column was used. Purified proteins were site-specifically biotinylated in a reaction with 200 μ M biotin, 500 μ M ATP, 500 μ M $MgCl_2$, 30 μ g/mL BirA, 0.1% (v/v) protease inhibitor cocktail and not more than 100 μ M of the protein-AviTag substrate. The reactions were incubated at 30 °C for 2 hours and biotinylated proteins then purified by size-exclusion chromatography.

Phage panning

A validated, synthetic, phage-displayed antibody library²⁴ was panned on SARS-CoV-2 spike RBD in solution. In each round, phage library was first depleted on neutravidin immobilized in wells of a 96 Maxisorp plate from a 2 μ g/mL solution incubated with shaking overnight at 4 °C, then incubated with 50 nM biotinylated RBD in solution for two hours at RT. Protein-phage complexes were captured in wells coated with neutravidin as above for 15 min at RT, then washed with 1X PBS pH7.4 containing 0.05% Tween and phage eluted for 5 min with 0.1 M HCl before neutralizing with 1M Tris pH 8.0. Eluted phage were amplified, purified, then panned against target for a total of 5 rounds, before isolation, amplification and sequencing of individual phage clones as previously described²⁴.

Enzyme linked immunosorbent assays

For ELISAs, plates were coated with neutravidin, as above, then blocked with 0.2% BSA in PBS for 1 hr. Biotinylated target protein was captured from solution by incubation in neutravidin-coated and BSA-blocked wells for 15 min with shaking at RT before addition and 30 min incubation of binding phage or antibody. Plates were washed then incubated with an appropriate secondary antibody before development with TB substrate as described³⁵.

Tetravalent Antibody Construction

DNA fragments encoding heavy chain Fab regions (VH-CH1; terminating at threonine 238, Kabat numbering) were amplified by PCR from the IgG expression constructs. Tetravalent antibody constructs were generated by fusing these fragments with their respective IgG heavy

chain in the pSCSTa mammalian expression vector using Gibson assembly (NEB). Fab-IgG constructs were arranged by fusing a heavy chain Fab domain to the N-terminus of the IgG via a S(G4S)₃ linker. IgG-Fab constructs were arranged by fusing a heavy chain Fab domain to the C-terminus using a G(G4S)₂GGGTG linker. For both formats, the Fc region terminated at glycine 447 (Kabat numbering).

Antibody Production

IgG and tetravalent antibodies were produced in Expi293F (ThermoFisher) by transient transfection, by diluting heavy and light chain construct DNA in OptiMem serum-free media (Gibco) before the addition of and incubation with FectoPro (Polyplus Transfection) for 10 min. For IgG expression, equivalent amounts of plasmids encoding heavy chain and light chains were transfected, whereas for tetravalent modalities, a ratio of 2:1 light chain to heavy chain plasmids was used. Following addition of the DNA complex to Expi293F cell and a 5-day expression period, antibodies were purified using rProtein A Sepharose (GE Healthcare), then buffer exchanged and concentrated using Amicon Ultra-15 Centrifugal Filter devices (Millipore). IgGs were stored in PBS (Gibco), while tetravalent antibodies were stored in a 10 mM L-Histidine, 0.9% sucrose, 140 mM NaCl, pH 6.0 buffer.

Size-exclusion chromatography

Fifty micrograms of protein were injected onto a TSKgel BioAssist G3SWxl (Tosoh) fitted with a guard column using an NGC chromatography system and a C96 autosampler (Biorad). The column was preequilibrated in a PBS mobile phase and protein retention was monitored by absorbance at 215 nm during a 1.5 CV isocratic elution in PBS.

Biolayer interferometry

The binding kinetics and estimation of apparent affinity (K_D) of antibodies against SARS CoV-2 spike RBD were determined by biolayer interferometry experiments performed on an Octet HTX instrument (ForteBio) at 1000 rpm and 25 °C. Biotinylated CoV-2 spike protein was first captured on streptavidin biosensors from a 2 µg/mL solution to achieve a binding response of 0.4-0.6 nm and unoccupied sites quenched with 100 µg/mL biotin. Antibodies were diluted with assay buffer

(PBS, 1% BSA, 0.05% Tween 20) and 67 nM of an unrelated biotinylated protein of similar size was used as negative control. Following equilibration with assay buffer, loaded biosensors were dipped for 600 s into wells containing 3-fold serial dilutions of each antibody from 67 nM and subsequently were transferred for 600 s back into assay buffer. Binding response data were reference subtracted and were fitted with 1:1 binding model using ForteBio's Octet Systems software 9.0.

Differential scanning fluorimetry

Thermostability of expressed antibodies were determined by differential scanning fluorimetry (DSF) using Sypro Orange as described³⁶ instead using a 1 μ M solution of antibody and temperature range from 25-100 °C in 0.5° increments.

Generation of SARS-CoV-2 pseudovirus

To generate SARS-CoV-2 pseudovirus, human embryonic kidney 293 (HEK 293)(ATCC) cells were seeded in a 6-well plate at 0.3×10^6 cells/well in DMEM (ThermoFisher) supplemented with 10% FBS and 1% penicillin-streptomycin (Gibco) and grown overnight at 37 °C, 5% CO₂. HEK 293 cells were then co-transfected with 1 μ g of pNL4-3.luc.R-E- plasmid (luciferase expressing HIV-1 with defective envelop protein) (NIH AIDS Reagent Program) and 0.06 μ g of CMV-promoter driven plasmid encoding SARS-CoV-2 wild type or mutant spike variants using Lipofectamine™ 2000 transfection reagent (ThermoFisher). Pseudovirus was harvested by collecting supernatant 48 h after transfection and filter sterilized (0.44 μ m, Millipore Sigma, Cat. No. SLHA033SS).

Pseudovirus Entry Assay

HEK 293 cells (ATCC) stably over-expressing full-length human ACE2 protein were seeded in 96 well white polystyrene microplates (Corning, Cat. No. CLS3610) at 0.03×10^6 cells/well in DMEM (10% FBS and 1% Pen-Strep), and grown overnight at 37 °C, 5% CO₂. To test the inhibition of pseudovirus entry of antibodies, the desired concentrations of antibodies were mixed with pseudoviruses, incubated at room temperature for 10 min, and were used to infect cells. The cells were incubated at 37 °C, 5% CO₂ for 6 h, then the medium was replaced with fresh DMEM

(10% FBS and 1% Pen-Strep), and again every 24 h up to 72 h. To measure the luciferase signal (virus uptake), DMEM was removed and cells were replaced in DPBS (ThermoFisher) and mixed with an equal volume of ONE-Glo™ EX Luciferase Assay System (Promega). Relative luciferase units were measured using a BioTek Synergy Neo plate reader (BioTek Instruments Inc.). The data was then analyzed by GraphPad Prism Version 8.4.3 (GraphPad Software, LLC.).

SARS-CoV-2 focal reduction neutralization assay

SARS-CoV-2 strain 2019 n-CoV/USA_WA1/2020 was obtained from the Centers for Disease Control (USA) and Prevention (gift of Natalie Thornburg). Virus stocks were produced in Vero CCL81 cells (ATCC) and titrated by focus-forming assay on Vero E6 cells³⁷. Serial dilutions of mAbs were incubated with 10² focus-forming units (FFU) of SARS-CoV-2 for 1 h at 37°C. MAb-virus complexes were added to Vero E6 cell monolayers in 96-well plates and incubated at 37°C for 1 h. Subsequently, cells were overlaid with 1% (w/v) methylcellulose in MEM supplemented with 2% FBS. Plates were harvested 30 h later by removing overlays and fixed with 4% PFA in PBS for 20 min at room temperature. Plates were washed and sequentially incubated with 1 µg/mL of CR3022³⁸ anti-S antibody and HRP-conjugated goat anti-human IgG in PBS supplemented with 0.1% saponin and 0.1% BSA. SARS-CoV-2-infected cell foci were visualized using TrueBlue peroxidase substrate (KPL) and quantitated on an ImmunoSpot microanalyzer (Cellular Technologies). Data were processed using Prism software (GraphPad Prism 8.0).

SARS-CoV-2 micro neutralization assay

SARS-CoV-2 strain 2019-nCoV/Italy-INMI1 was obtained from the National Institute for Infectious Diseases Lazzaro Spallanzani IRCCS (Italy) and passaged in Vero E6 cells³⁹ before determining the tissue culture infectious dose (TCID50) as described⁴⁰. Antibodies were serially diluted two-fold in serum-free medium and mixed with an equal volume of 100X the TCID50/well SARS-CoV-2 virus then incubated at 37°C for 30 min. Sub-confluent Vero E6 cell monolayers in tissue culture plates were infected with virus-serum mixtures in duplicate and incubated at 37°C in % CO₂ for two days. The supernatant of each plate was then carefully discarded and cell viability

determined by crystal violet assay reading the absorbance at 595 nm (Synergy HTX Biotek) as described⁴¹.

X-ray crystallography

For the x-ray crystallographic work, the SARS-CoV-2 RBD (residues 328-528) was expressed with a C-terminal 6xHis tag from HEK293F GnT1-minus cells. The Fabs were expressed from HEK293F cells. The RBD was purified from the expression media by metal-affinity chromatography using Ni-NTA beads (Qiagen). The Fabs were purified from the expression media using rProtein A Sepharose Fast Flow beads (GE healthcare). The RBD was treated with endoglycosidase H⁴² and Carboxypeptidase A (Sigma-Aldrich), to remove the N-glycans and the C-terminal 6xHis tag. The RBD and Fabs were then further purified by ion-exchange and hydrophobic interaction chromatography. Before crystallization, the RBD-Fab complexes were purified using size-exclusion chromatography on a Superdex 200 Increase column (GE Healthcare). For both Fab 15033 and Fab 15033-7, the optimized crystallization conditions contained 1.2-1.6 M (NH₄)₂SO₄ and 8-18% glycerol. X-ray diffraction data were collected at 100 K on beamline 08IB-1 at the Canadian Light Source. The diffraction data were integrated and scaled using the XDS package⁴³. The structures were solved by molecular replacement using the program Phaser⁴⁴. A homology model of the VH-VL region was produced by the SysImm Repertoire Builder server (https://sysimm.org/rep_builder, <https://pubs.rsc.org/en/content/articlehtml/2019/me/c9me00020h>). The CDR loops were then deleted from this VH-VL model. The constant (CH1-CL) region search model and the RBD search model were both derived from PDB entry 6W41³⁸. The three models were used to solve the structure by molecular replacement. The atomic models were built using Coot⁴⁵ and refined with Phenix.refine⁴⁶.

FIGURES

Figure 1. Characterization of anti-RBD Abs by ELISA.

Figure 1

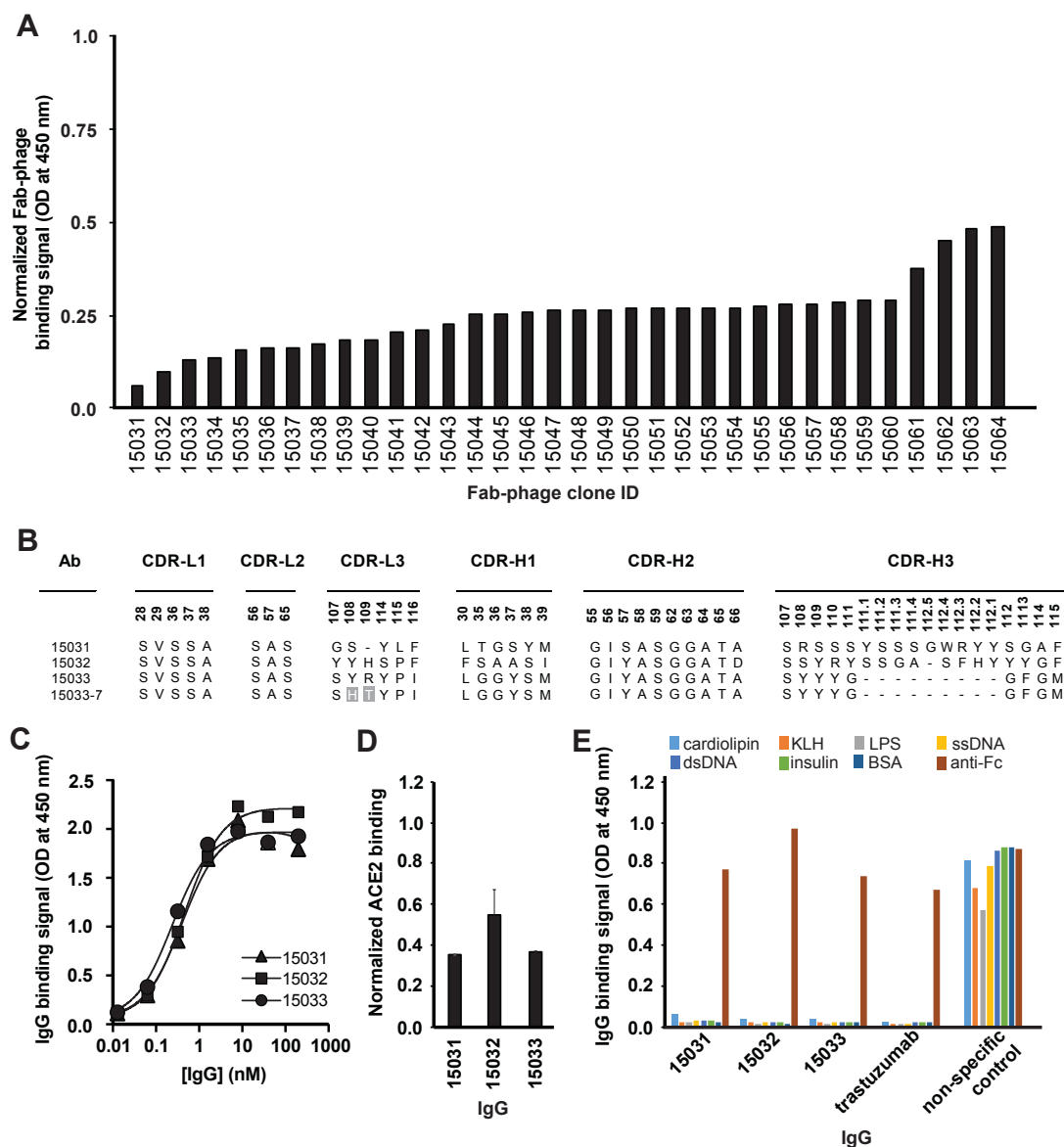


Figure 1. Characterization of anti-RBD Abs by ELISA. (A) Binding of unique Fab-phage clones (x-axis) to immobilized RBD blocked by solution-phase ACE2 (y-axis). Signal was normalized to the signal in the absence of ACE2. **(B)** CDR sequences of Abs for which the binding to RBD was strongly blocked by ACE2. Positions that are highly variable in the immune repertoire are shown and are numbered according to the IMGT nomenclature⁴⁷. Sequences in 15033-7 that differ from 15033 are shaded grey. **(C)** Serial dilutions of IgGs (x-axis) binding to immobilized S protein trimer (y-axis). The EC₅₀ values derived from the curves are shown in Table 1 and values are representative of 2 independent experiments. **(D)** Binding of biotinylated ACE2 (y-axis) to immobilized S protein blocked by solution-phase IgG (x-axis). Signal was normalized to the signal in the presence of a non-binding control IgG and error bars shown as the standard error of the mean of duplicate samples. **(E)** Assessment of non-specific binding (y-axis) of IgGs (x-axis) to immobilized antigens or a goat anti-human Fc Ab (positive control).

Figure 2. Structural analysis of Fabs bound to the RBD.

Figure 2

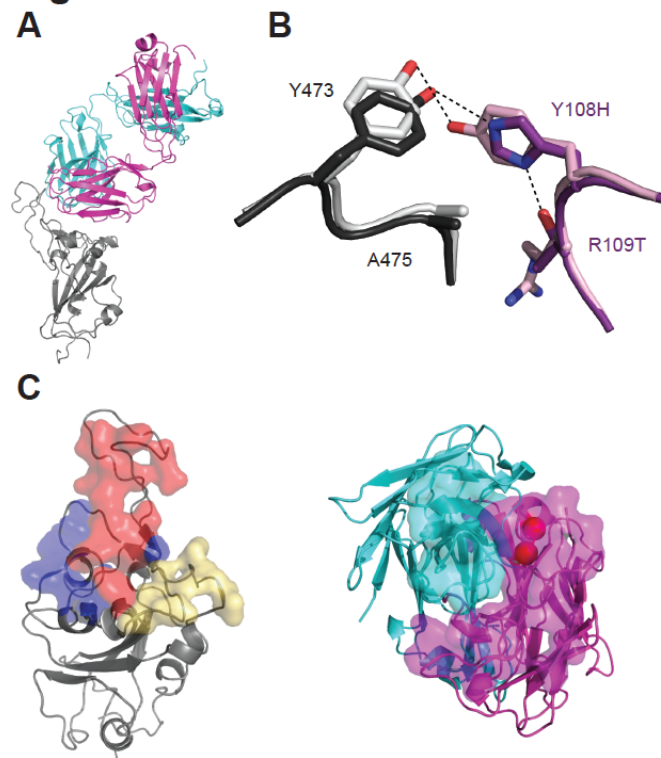


Figure 2. Structural analysis of Fabs bound to the RBD. (A) The crystal structure of Fab 15033-7 (light chain, magenta; heavy chain, cyan) in complex with the SARS-CoV-2 RBD (grey). (B) Side chain interactions between CDR-L3 residues and the RBD. Superposed CDR-L3 loops of Fabs 15033 and 15033-7 are colored light or dark purple, respectively, and the RBD residues they contact are colored light or dark grey, respectively. CDR-L3 residues are numbered with the sequence in Fab 15033 or 15033-7 to the left or right of the number, respectively. Hydrogen bonds are indicated by dashed lines. (C) The structural epitope and paratope. The RBD (left) and Fab 15033-7 (right) are shown in an open book view and residues within 4.0 Å of the cognate ligand are shown as colored surfaces. For the RBD, residues in the ACE2-binding site are also shown as colored surfaces, and the following color scheme was used: red, contacts with both Fab 15033-7 and ACE2; blue, contacts with Fab 15033-7 only; yellow, contacts with ACE2 only. Fab 15033-7 residues that contact the RBD are colored magenta or cyan if they reside in the light or heavy chain, respectively. The CDR-L3 residues that differ between 15033-7 and 15033 are shown as red spheres.

Figure 3. Design and characterization of tetravalent nAbs.

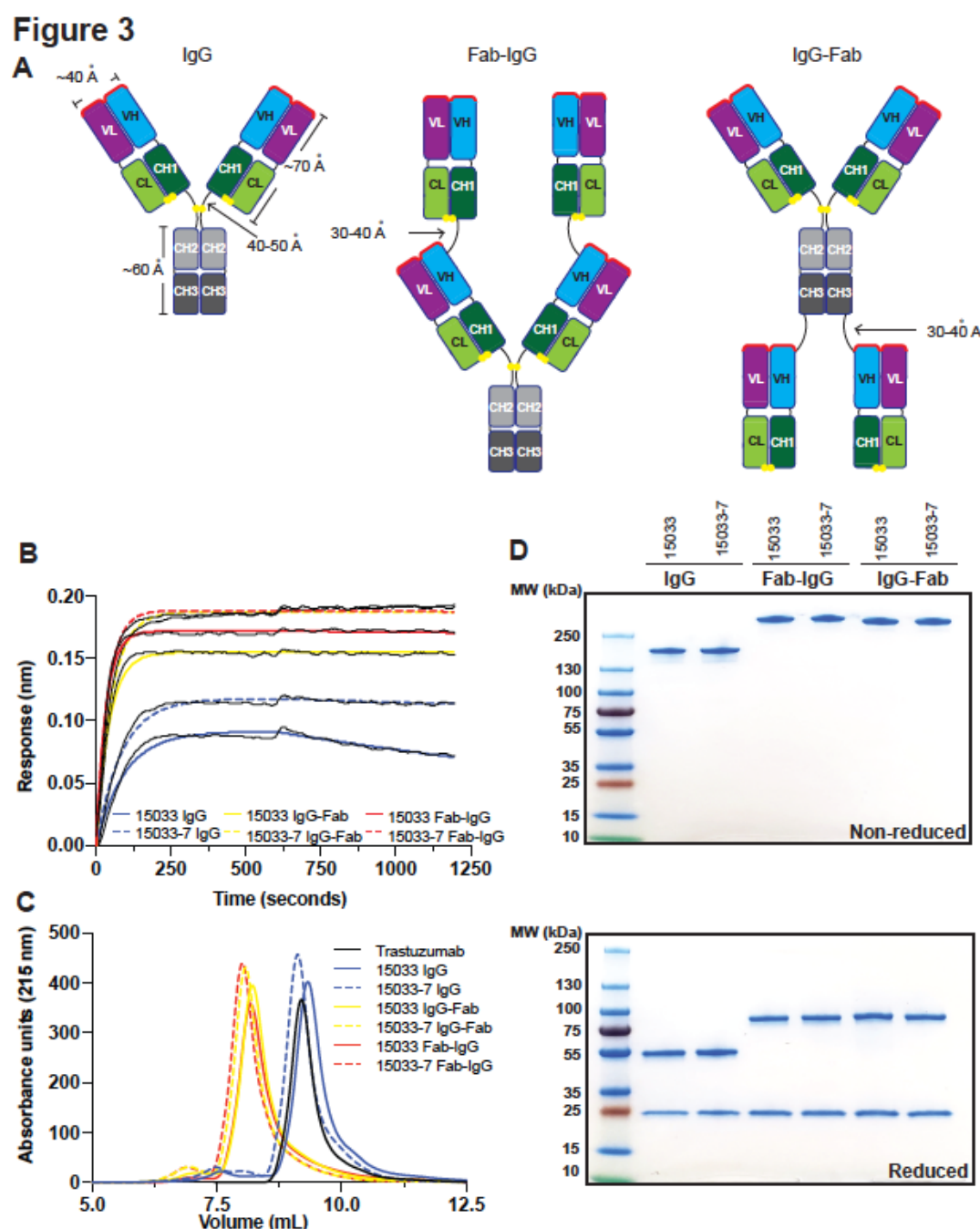


Figure 3. Design and characterization of tetravalent nAbs. (A) Schematic of the bivalent IgG format, and the tetravalent Fab-IgG and IgG-Fab formats. Paratopes are shown in red, linkers are shown in black, and disulfide bonds are shown as yellow spheres. **(B)** BLI sensor traces for nAbs binding to immobilized S protein trimer. **(C)** Analytical gel filtration of nAbs. **(D)** SDS-PAGE analysis of nAbs under non-reducing (top) or reducing conditions (bottom) and are representative of n=2 independent preparations.

Figure 4. Neutralization of SARS-CoV-2 virus and pseudotyped VLPs.

Figure 4

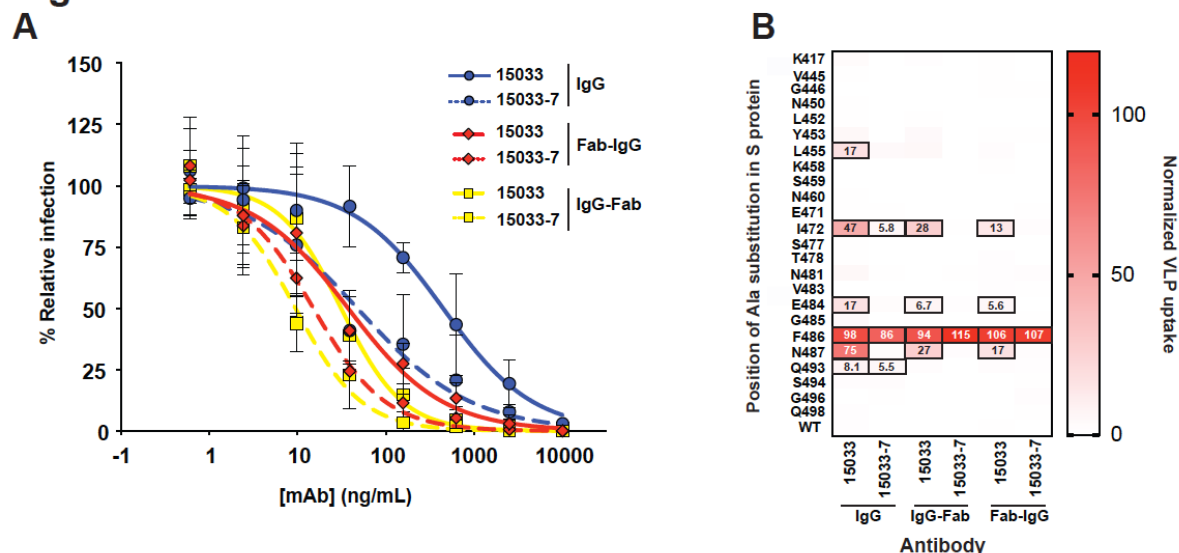


Figure 4. Neutralization of SARS-CoV-2 virus and pseudotyped VLPs. (A) Neutralization of SARS-CoV-2 strain 2019 n-CoV/USA_WA1/2020 by bivalent and tetravalent nAbs. The virus was pre-treated with serial dilutions of nAb (x-axis) and infection of ACE2-expressing Vero E6 cells was measured relative to untreated control (y-axis). Samples were run in duplicate and results are representative of n=2 independent experiments. Error bars indicate standard error of the mean. **(B)** Neutralization of a panel of pseudotyped VLPs displaying SARS-CoV-2 S proteins with single alanine mutations in or near the ACE2-binding site (y-axis). The VLPs were treated with 50 nM of the indicated nAb (x-axis) and uptake by ACE2-expressing HEK-293 cells was measured in triplicate and results are representative of n=2 independent experiments. The heat map shows uptake normalized to uptake in the absence of nAb. Boxed cells indicate VLPs that represented escape mutants for a given nAb, as defined by >5% uptake with nAb treatment compared with untreated control (the percent uptake is shown in each cell).

Table 1. Characteristics of lead IgG and tetravalent antibodies

ID	Format	Yield (mg·L ⁻¹)	EC ₅₀ (nM)	k _{on} (10 ⁵ M ⁻¹ s ⁻¹)	k _{off} (10 ⁻⁵ s ⁻¹)	Apparent K _D (pM)	Viral IC ₅₀ (ng·mL ⁻¹)	Viral IC ₅₀ (pM)	Spike VLP EC ₅₀ (nM)	SEC Elution volume (mL)	Mono- dispersity (%)	Tm2 (°C)
trastuzumab	IgG	303	NA	NA	NA	NA	NA	NA	NA	9.20	>95	79.5
15033	IgG	207	0.24	17	50	300	523	3540	0.44	9.34	91	81
15033-7	IgG	165	0.09	18	7	39	118	790	0.37	9.13	95	81
15033	Fab-IgG	214	0.18	46	1.5	3	48	320	0.27	8.22	>95	87
15033-7	Fab-IgG	194	0.14	40	0.8	2	15	100	0.35	8.02	93	85.5
15033	IgG-Fab	166	0.11	36	1.9	5	51	340	0.27	8.22	>95	87
15033-7	IgG-Fab	118	0.15	30	<0.1	<1	9.1	61	0.47	8.09	93	85

REFERENCES

1. Beigel JH, Tomashek KM, Dodd LE, Mehta AK, Zingman BS, Kalil AC, Hohmann E, Chu HY, Luetkemeyer A, Kline S, et al. Remdesivir for the Treatment of Covid-19 — Preliminary Report. *N Engl J Med* 2020;
2. Boulware DR, Pullen MF, Bangdiwala AS, Pastick KA, Lofgren SM, Okafor EC, Skipper CP, Nascene AA, Nicol MR, Abassi M, et al. A Randomized Trial of Hydroxychloroquine as Postexposure Prophylaxis for Covid-19. *N Engl J Med* 2020; 383:517–25.
3. Robbiani DF, Gaebler C, Muecksch F, Lorenzi JCC, Wang Z, Cho A, Agudelo M, Barnes CO, Gazumyan A, Finkin S, et al. Convergent antibody responses to SARS-CoV-2 in convalescent individuals. *Nature* 2020; 584:437–42.
4. Long QX, Tang XJ, Shi QL, Li Q, Deng HJ, Yuan J, Hu JL, Xu W, Zhang Y, Lv FJ, et al. Clinical and immunological assessment of asymptomatic SARS-CoV-2 infections. *Nat Med* 2020; 26:1200–4.
5. Li L, Zhang W, Hu Y, Tong X, Zheng S, Yang J, Kong Y, Ren L, Wei Q, Mei H, et al. Effect of Convalescent Plasma Therapy on Time to Clinical Improvement in Patients With Severe and Life-threatening COVID-19: A Randomized Clinical Trial. *JAMA* 2020;
6. Shen C, Wang Z, Zhao F, Yang Y, Li J, Yuan J, Wang F, Li D, Yang M, Xing L, et al. Treatment of 5 Critically Ill Patients with COVID-19 with Convalescent Plasma. *JAMA - J Am Med Assoc* 2020; 323:1582–9.
7. Duan K, Liu B, Li C, Zhang H, Yu T, Qu J, Zhou M, Chen L, Meng S, Hu Y, et al. Effectiveness of convalescent plasma therapy in severe COVID-19 patients. *Proc Natl Acad Sci U S A* 2020; 117:9490–6.
8. Alsoussi WB, Turner JS, Case JB, Zhao H, Schmitz AJ, Zhou JQ, Chen RE, Lei T, Rizk AA, McIntire KM, et al. A Potently Neutralizing Antibody Protects Mice against SARS-CoV-2 Infection. *J Immunol* 2020; 205:915–22.
9. Shi R, Shan C, Duan X, Chen Z, Liu P, Song J, Song T, Bi X, Han C, Wu L, et al. A human neutralizing antibody targets the receptor-binding site of SARS-CoV-2. *Nature* 2020; 584:120–4.
10. Sui J, Li W, Murakami A, Tamin A, Matthews LJ, Wong SK, Moore MJ, Tallarico ASC,

- 632 Olurinde M, Choe H, et al. Potent neutralization of severe acute respiratory syndrome
633 (SARS) coronavirus by a human mAb to S1 protein that blocks receptor association. *Proc*
634 *Natl Acad Sci U S A* 2004; 101:2536–41.
- 635 11. Zhu Z, Chakraborti S, He Y, Roberts A, Sheahan T, Xiao D, Hensley LE, Prabakaran P, Rockx
636 B, Sidorov IA, et al. Potent cross-reactive neutralization of SARS coronavirus isolates by
637 human monoclonal antibodies. *Proc Natl Acad Sci U S A* 2007; 104:12123–8.
- 638 12. Meulen J Ter, Bakker ABH, Brink EN Van Den, Weverling GJ, Martina BEE, Haagmans BL,
639 Kuiken T, Kruif J De, Preiser W, Spaan W, et al. Human monoclonal antibody as
640 prophylaxis for SARS coronavirus infection in ferrets. *Lancet* 2004; 363:2139–41.
- 641 13. Corti D, Zhao J, Pedotti M, Simonelli L, Agnihothram S, Fett C, Fernandez-Rodriguez B,
642 Foglierini M, Agatic G, Vanzetta F, et al. Prophylactic and postexposure efficacy of a
643 potent human monoclonal antibody against MERS coronavirus. *Proc Natl Acad Sci U S A*
644 2015; 112:10473–8.
- 645 14. Klein S, Cortese M, Winter SL, Wachsmuth-Melm M, Neufeldt CJ, Cerikan B, Stanifer ML,
646 Boulant S, Bartenschlager R, Chlanda P. SARS-CoV-2 structure and replication
647 characterized by in situ cryo-electron tomography. *bioRxiv* 2020; :2020.06.23.167064.
- 648 15. Ke Z, Oton J, Qu K, Cortese M, Zila V, McKeane L, Nakane T, Zivanov J, Neufeldt CJ,
649 Cerikan B, et al. Structures and distributions of SARS-CoV-2 spike proteins on intact
650 virions. *Nature* 2020; :1–7.
- 651 16. Hoffmann M, Kleine-Weber H, Schroeder S, Mü MA, Drosten C, Pö S. SARS-CoV-2 Cell
652 Entry Depends on ACE2 and TMPRSS2 and Is Blocked by a Clinically Proven Protease
653 Inhibitor. *Cell* 2020; 181:271-280.e8.
- 654 17. Hansen J, Baum A, Pascal KE, Russo V, Giordano S, Wloga E, Fulton BO, Yan Y, Koon K,
655 Patel K, et al. Studies in humanized mice and convalescent humans yield a SARS-CoV-2
656 antibody cocktail. *Science* 2020; 369:1010–4.
- 657 18. Pinto D, Park Y-J, Beltramello M, Walls AC, Tortorici MA, Bianchi S, Jaconi S, Culap K,
658 Zatta F, Marco A De, et al. Cross-neutralization of SARS-CoV-2 by a human monoclonal
659 SARS-CoV antibody.
- 660 19. Cao Y, Su B, Guo X, Sun W, Deng Y, Bao L, Zhu Q, Zhang X, Zheng Y, Geng C, et al. Potent

- Neutralizing Antibodies against SARS-CoV-2 Identified by High-Throughput Single-Cell Sequencing of Convalescent Patients' B Cells. *Cell* 2020; 182:73-84.e16.
20. Rogers TF, Zhao F, Huang D, Beutler N, Burns A, He WT, Limbo O, Smith C, Song G, Woehl J, et al. Isolation of potent SARS-CoV-2 neutralizing antibodies and protection from disease in a small animal model. *Science* (80-) 2020; 369:956–63.
21. Wan J, Xing S, Ding L, Wang Y, Gu C, Wu Y, Rong B, Li C, Wang S, Chen K, et al. Human-IgG-Neutralizing Monoclonal Antibodies Block the SARS-CoV-2 Infection. *Cell Rep* 2020; 32.
22. Noy-Porat T, Makdasi E, Alcalay R, Mechaly A, Levy Y, Bercovich-Kinori A, Zauberman A, Tamir H, Yahalom-Ronen Y, Israeli M, et al. A panel of human neutralizing mAbs targeting SARS-CoV-2 spike at multiple epitopes. *Nat Commun* 2020; 11:1–7.
23. Wec AZ, Wrapp D, Herbert AS, Maurer DP, Haslwanter D, Sakharkar M, Jangra RK, Dieterle ME, Lilov A, Huang D, et al. Broad neutralization of SARS-related viruses by human monoclonal antibodies. *Science* (80-) 2020; 369:731–6.
24. Persson H, Ye W, Wernimont A, Adams JJ, Koide A, Koide S, Lam R, Sidhu SS. CDR-H3 diversity is not required for antigen recognition by synthetic antibodies. *J Mol Biol* 2013; 425:803–11.
25. Mouquet H, Scheid JF, Zoller MJ, Krogsgaard M, Ott RG, Shukair S, Artyomov MN, Pietzsch J, Connors M, Pereyra F, et al. Polyreactivity increases the apparent affinity of anti-HIV antibodies by heterologation. *Nature* 2010; 467:591–5.
26. Jain T, Sun T, Durand S, Hall A, Houston NR, Nett JH, Sharkey B, Bobrowicz B, Caffry I, Yu Y, et al. Biophysical properties of the clinical-stage antibody landscape. *Proc Natl Acad Sci U S A* 2017; 114:944–9.
27. Jones BE, Brown-Augsburger PL, Corbett KS, Westendorf K, Davies J, Cujec TP, Wiethoff CM, Blackbourne JL, Heinz BA, Foster D, et al. Title: LY-CoV555, a rapidly isolated potent neutralizing antibody, provides protection in a non-human primate model of SARS-CoV-2 infection.
28. Daszak P, Olival KJ, Li H. A strategy to prevent future epidemics similar to the 2019-nCoV outbreak. *Biosaf Heal* 2020; 2:6–8.

29. Shi Z, Hu Z. A review of studies on animal reservoirs of the SARS coronavirus. *Virus Res* 2008; 133:74–87.
30. Hornsby M, Paduch M, Miersch S, Sääf A, Matsuguchi T, Lee B, Wypisniak K, Doak A, King D, Usatyuk S, et al. A high through-put platform for recombinant antibodies to folded proteins. *Mol Cell Proteomics* 2015; 14:2833–47.
31. Li Z, Michael IP, Zhou D, Nagy A, Rini JM. Simple piggyBac transposon-based mammalian cell expression system for inducible protein production. *Proc Natl Acad Sci U S A* 2013; 110:5004–9.
32. Tao Y, Strelkov S V, Mesyanzhinov V V, Rossmann MG. Structure of bacteriophage T4 fibrin: a segmented coiled coil and the role of the C-terminal domain. *Structure* 1997; 5:789–98.
33. Fairhead M, Howarth M. Site-specific biotinylation of purified proteins using BirA. *Methods Mol Biol* 2015; 1266:171–84.
34. Pallesen J, Wang N, Corbett KS, Wrapp D, Kirchdoerfer RN, Turner HL, Cottrell CA, Becker MM, Wang L, Shi W, et al. Immunogenicity and structures of a rationally designed prefusion MERS-CoV spike antigen. *Proc Natl Acad Sci U S A* 2017; 114:E7348–57.
35. Miersch S, Maruthachalam BV, Geyer CR, Sidhu SS. Structure-Directed and Tailored Diversity Synthetic Antibody Libraries Yield Novel Anti-EGFR Antagonists. *ACS Chem Biol* 2017; 12:1381–9.
36. Niedziela-Majka A, Kan E, Weissburg P, Mehra U, Sellers S, Sakowicz R. High-throughput screening of formulations to optimize the thermal stability of a therapeutic monoclonal antibody. *J Biomol Screen* 2015; 20:552–9.
37. Case JB, Rothlauf PW, Chen RE, Liu Z, Zhao H, Kim AS, Bloyet LM, Zeng Q, Tahan S, Droit L, et al. Neutralizing Antibody and Soluble ACE2 Inhibition of a Replication-Competent VSV-SARS-CoV-2 and a Clinical Isolate of SARS-CoV-2. *Cell Host Microbe* 2020; 28:475-485.e5.
38. Yuan M, Wu NC, Zhu X, Lee CCD, So RTY, Lv H, Mok CKP, Wilson IA. A highly conserved cryptic epitope in the receptor binding domains of SARS-CoV-2 and SARS-CoV. *Science* 2020; 368:630–3.
39. Capobianchi MR, Rueca M, Messina F, Giombini E, Carletti F, Colavita F, Castilletti C, Lalle

- E, Bordi L, Vairo F, et al. Molecular characterization of SARS-CoV-2 from the first case of COVID-19 in Italy. *Clin. Microbiol. Infect.* 2020; 26:954–6.
40. A simple method of estimating fifty percent endpoints – ScienceOpen [Internet]. [cited 2020 Oct 29]; Available from: <https://www.scienceopen.com/document?vid=21401620-94ad-4100-a3e1-56741c541ab6>
41. Feoktistova M, Geserick P, Leverkus M. Crystal violet assay for determining viability of cultured cells. *Cold Spring Harb Protoc* 2016; 2016:343–6.
42. Primary structure of the Streptomyces enzyme endo-beta-N-acetylglucosaminidase H - PubMed [Internet]. [cited 2020 Oct 30]; Available from: <https://pubmed.ncbi.nlm.nih.gov/6429133/>
43. Kabsch W. XDS. *Acta Crystallogr D Biol Crystallogr* 2010; 66:125–32.
44. McCoy AJ, Grosse-Kunstleve RW, Adams PD, Winn MD, Storoni LC, Read RJ. Phaser crystallographic software. *J Appl Crystallogr* 2007; 40:658–74.
45. Emsley P, Lohkamp B, Scott WG, Cowtan K. Features and development of Coot. *Acta Crystallogr Sect D Biol Crystallogr* 2010; 66:486–501.
46. Afonine P V., Grosse-Kunstleve RW, Echols N, Headd JJ, Moriarty NW, Mustyakimov M, Terwilliger TC, Urzhumtsev A, Zwart PH, Adams PD. Towards automated crystallographic structure refinement with phenix.refine. *Acta Crystallogr Sect D Biol Crystallogr* 2012; 68:352–67.
47. Lefranc MP, Pommié C, Ruiz M, Giudicelli V, Foulquier E, Truong L, Thouvenin-Contet V, Lefranc G. IMGT unique numbering for immunoglobulin and T cell receptor variable domains and Ig superfamily V-like domains. *Dev Comp Immunol* 2003; 27:55–77.

